Title: A Lethal Genetic Incompatibility between Naturally Hybridizing Species in Mitochondrial Complex I

Authors: Benjamin M. Moran[1,2]*, Cheyenne Y. Payne[1,2], Daniel L. Powell[1,2], Erik N. K. Iverson[3], Alex E. Donny[1], Shreya M. Banerjee[1], Quinn K. Langdon[1], Theresa R. Gunn[1], Rebecca A. Rodriguez-Soto[1], Angel Madero[1], John J. Baczenas[1], Korbin M. Kleczko[1], Fang Liu[4], Rowan Matney[4], Kratika Singhal[4], Ryan D. Leib[4], Osvaldo Hernandez-Perez[2], Russell Corbett-Detig[5,6], Judith Frydman[1,7], Casey Gifford[7], Manfred Schartl[8,9], Justin C. Havird[3], Molly Schumer[1,2,10]*

Affiliations:

[1]Department of Biology, Stanford University, Stanford, CA, USA

[2]Centro de Investigaciones Científicas de las Huastecas "Aguazarca", A.C., Calnali, Hidalgo, Mexico

[3]Department of Integrative Biology, University of Texas, Austin, TX, USA

[4]Stanford University Mass Spectrometry Core, Stanford University, Stanford, CA, USA

[5]Genomics Institute, University of California, Santa Cruz, CA, USA

[6]Department of Biomolecular Engineering, University of California, Santa Cruz, CA, USA

[7]Department of Genetics and Pediatrics, Stanford University, Stanford, CA, USA

[8]The Xiphophorus Genetic Stock Center, Texas State University, San Marcos, TX 78666

[9]Developmental Biochemistry, Biozentrum, University of Würzburg, 97070 Würzburg, Germany

[10]Hanna H. Gray Fellow, Howard Hughes Medical Institute, Stanford, CA, USA

*Correspondence: benmoran@stanford.edu, schumer@stanford.edu

Abstract

The evolution of reproductive barriers is the first step in the formation of new species and can help us understand the diversification of life on Earth. These reproductive barriers often take the form of "hybrid incompatibilities," where alleles derived from two different species no longer interact properly in hybrids. Theory predicts that hybrid incompatibilities may be more likely to arise at rapidly evolving genes and that incompatibilities involving multiple genes should be common, but there has been sparse empirical data to evaluate these predictions. Here, we describe a mitonuclear incompatibility involving three genes in physical contact within respiratory Complex I in naturally hybridizing swordtail fish species. Individuals homozygous for specific mismatched protein combinations fail to complete embryonic development or die as juveniles, while those heterozygous for the incompatibility have reduced function of Complex I and unbalanced representation of parental alleles in the mitochondrial proteome. We find that the impacts of different genetic interactions on survival are non-additive, highlighting subtle complexity in the genetic architecture of hybrid incompatibilities. We document the evolutionary history of the genes involved, showing for the first time that an incompatibility has been transferred between species via hybridization. This work thus provides the first glimpse into the genetic architecture, physiological impacts, and evolutionary origin of a complex incompatibility impacting naturally hybridizing species.

Introduction

Biologists have long been fascinated by the question of how new species are formed and what mechanisms maintain isolation between them. One key factor in the formation and maintenance of new species is the emergence of genetic incompatibilities that reduce viability or fertility in hybrids[1]. As originally described by the Dobzhansky-Muller model of hybrid incompatibility[2,3], the unique sets of mutations that accumulate in diverging species may interact poorly when they are brought together in hybrids, given that they have never been tested against one another by selection. Due to the technical challenges of identifying these interactions[4], only around a dozen genes involved in hybrid incompatibilities have been precisely mapped[5] and exploration of the functional and evolutionary causes of hybrid incompatibilities has been limited to a small number of cases in model organisms[4].

This knowledge gap leaves key predictions about the evolutionary processes that drive the emergence of hybrid incompatibilities untested. For one, theory suggests that incompatibilities should be more common within dense gene networks, both because genes involved in such interactions are expected to be tightly co-evolving and because the number of potentially incompatible genotypes explodes as the complexity of the genetic interaction increases[6,7]. Consistent with this prediction, mutagenesis experiments have highlighted the sensitivity of multi-protein interactions to changes in any of their components[6]. However, genetic interactions are notoriously difficult to detect empirically except in systems with especially powerful genetic tools[8], and this problem is exacerbated with complex genetic interactions[9,10]. Such technical challenges may explain the rarity of incompatibilities involving three or more genes in the empirical literature[6] (but see[8,11–14]).

68 Another open question is the degree to which the genes that become involved in hybrid
69 incompatibilities are predictable from their molecular or evolutionary properties. Researchers
70 have proposed for decades that rapid molecular evolution will increase the rate at which
71 incompatibilities accumulate between species[4,5,15]. While several incompatibilities identified to
72 date involve genes showing signatures of positive selection, it is unclear how unusual rates of
73 protein evolution are in genes involved in hybrid incompatibilities relative to the genomic
74 background[5,15]. The mitochondrial genome, in particular, has been proposed as a hotspot for the
75 accumulation of genetic incompatibilities[16,17], due to substitution rates up to 25× higher than the
76 nuclear genome in many animals[18–20] and the potential for sexually antagonistic selection driven
77 by its predominantly maternal inheritance[21–23], among other factors[24]. At the same time, nuclear
78 and mitochondrial gene products must directly interact with each other in key steps of ATP
79 synthesis, increasing the likelihood of coevolution between these genomes[25,26]. These molecular
80 and evolutionary factors suggest that interactions between mitochondrial- and nuclear-encoded
81 proteins could play an outsized role in the emergence of hybrid incompatibilities[16]. Crosses in
82 numerous species have shown that hybrid viability often depends on the identity of the maternal
83 species[27–30], providing indirect evidence for the prevalence of mitonuclear incompatibilities.
84 However, the field has struggled to move beyond these coarse-scale patterns, as few studies have
85 successfully mapped mitonuclear incompatibilities to the single gene level[31–34] and none of those
86 identified to date have been studied in species that naturally hybridize.
87 As we begin to identify the individual genes underlying hybrid incompatibilities, the next
88 frontier is evaluating the processes that drive their evolution. Over the past two decades, it has
89 become abundantly clear that hybridization is exceptionally common in species groups where it
90 was once thought to be rare[35,36]. As such, we now appreciate how frequently species derive genes

from their relatives, and in many cases are a patchwork of ancestry from several genomes due to historical hybridization[37–39]. The impact of these dynamics on the evolution of hybrid incompatibilities have been poorly investigated[40] since the foundational theory in this area was developed before the ubiquity of hybridization was fully appreciated[7].

Here, we use an integrative approach to precisely map the genetic basis and physiological impacts of a lethal mitonuclear hybrid incompatibility in swordtail fish and uncover its evolutionary history. The sister species *Xiphophorus birchmanni* and *X. malinche* began hybridizing in the last ~100 generations in multiple river systems[41] after premating barriers were disrupted by habitat disturbance[42], and are a powerful system to study the emergence of hybrid incompatibilities in young species. Despite their recent divergence[43] (~250,000 generations; 0.5% divergence per basepair), some hybrids between *X. birchmanni* and *X. malinche* experience strong selection against incompatibilities[43,44]. One incompatibility causing melanoma has been previously mapped in this system and population genetic patterns suggest that dozens may be segregating in natural hybrid populations[43–46]. Moreover, the ability to generate controlled crosses[47,48] and the development of high-quality genomic resources[46,49] makes this system particularly tractable for identifying hybrid incompatibilities and characterizing their evolution in natural populations. Leveraging data from controlled laboratory crosses and natural hybrid populations, we pinpoint two nuclear-encoded *X. birchmanni* genes that are lethal when mismatched with the *X. malinche* mitochondria in hybrids, explore the developmental and physiological effects of this incompatibility, and trace its evolutionary history.

114 **Admixture Mapping Reveals a Lethal Mitonuclear Incompatibility**

115

116 To identify loci under selection in *X. birchmanni* × *X. malinche* hybrids, we generated
117 ~1X low-coverage whole-genome sequence data for 943 individuals from an F_2 laboratory cross
118 and 359 wild-caught hybrid adults, and applied a hidden Markov model to data at 629,661
119 ancestry-informative sites along the genome to infer local ancestry (~1 informative site per
120 kb[45,50]; Methods, Supplementary Information 1.1.1–1.1.4). Using these results, we found
121 evidence for a previously unknown incompatibility between the nuclear genome of *X.*
122 *birchmanni* and the mitochondrial genome of *X. malinche* (Supplementary Information 1.1.5–
123 1.1.10). Our first direct evidence for this incompatibility came from controlled laboratory crosses
124 (Methods, Supplementary Information 1.1.1). Because the cross is largely unsuccessful in the
125 opposite direction, all lab-bred hybrids were the offspring of F_1 hybrids generated between *X.*
126 *malinche* females and *X. birchmanni* males and harbored a mitochondrial haplotype derived from
127 the *X. malinche* parent species. Offspring of F_1 intercrosses are expected to derive on average
128 50% of their genome from each parent species. This expectation is satisfied genome-wide and
129 locally along most chromosomes in F_2 hybrids (on average 50.3% *X. malinche* ancestry; Fig. S1).
130 However, we detected six segregation distorters genome-wide[48], with the most extreme signals
131 falling along a 6.5 Mb block of chromosome 13 and an 4.9 Mb block of chromosome 6 (Fig. 1A;
132 Fig. 1D).

133 Closer examination of genotypes in the chromosome 13 region showed that almost none
134 of the surviving individuals harbored homozygous *X. birchmanni* ancestry in a 3.75 Mb
135 subregion (Fig. 1C; Fig. S2; 0.1% observed vs 25% expected). This pattern is unexpected even in
136 the case of a lethal incompatibility involving only nuclear loci (where simulations indicate that

137 we should recover homozygous *X. birchmanni* ancestry in ~10% of surviving individuals;
138 Supplementary Information 1.1.1) but is consistent with a lethal mitonuclear incompatibility.
139 Using approximate Bayesian computation (ABC) approaches we inferred what strength of
140 selection against *X. birchmanni* ancestry in this region was consistent with the genotypes and
141 ancestry deviations observed. We estimated posterior distributions of selection and dominance
142 coefficients and inferred that selection on this genotype in F_2s is largely recessive and essentially
143 lethal (maximum a posteriori estimate $h = 0.12$ and $s = 0.996$, 95% credible interval $h = 0.010$–
144 0.194 and $s = 0.986$–0.999; Fig. 1B; Fig. S3; Methods; Supplementary Information 1.2.1–1.2.2).
145 The degree of segregation distortion observed in F_2 individuals on chromosome 6 is also
146 surprising (Fig. 1D). Only 3% of individuals harbor homozygous *X. birchmanni* ancestry in this
147 region (compared to 0.1% in the chromosome 13 region and 25% on average at other loci across
148 the genome; Fig 1F), which is again lower than expected for a nuclear-nuclear hybrid
149 incompatibility (Supplementary Information 1.1.1). ABC approaches indicate that selection on
150 homozygous *X. birchmanni* ancestry on chromosome 6 is also severe (maximum a posteriori
151 estimate $h = 0.09$ and $s = 0.91$, 95% credible interval interval $h = 0.01$–0.21 and $s = 0.87$–0.94;
152 Fig. 1E, Fig. S3, Supplementary Information 1.2.2). Thus, our F_2 data show that homozygous *X.*
153 *birchmanni* ancestry in regions of either chromosome 13 or chromosome 6 is almost completely
154 lethal in hybrids with *X. malinche* mitochondria (Fig. 1H).
155 To formally test for the presence of a mitonuclear incompatibility involving chromosome
156 13 and chromosome 6, or elsewhere in the genome, we leveraged data from natural hybrid
157 populations. Most naturally occurring *X. birchmanni* × *malinche* hybrid populations are fixed for
158 mitochondrial haplotypes from one parental species (Supplementary Information 1.1.2, 1.1.6).
159 However, a few populations segregate for the mitochondrial genomes of both parental types, and

160 we focused on one such population (the "Calnali Low" population, hereafter the admixture
161 mapping population). Admixture mapping for associations between nuclear genotype and
162 mitochondrial ancestry (after adjusting for expected covariance due to genome-wide ancestry[44])
163 revealed two genome-wide significant peaks and one peak that approached genome-wide
164 significance (Fig. 1G, Table S1–S3). The strongest peak of association spanned approximately
165 77 kb and fell within the region of chromosome 13 identified using F_2 crosses (Fig. 1G). This
166 peak was also replicated in another hybrid population (Fig. S4; Methods, Supplementary
167 Information 1.1.5) and contains only three genes: the NADH dehydrogenase ubiquinone iron-
168 sulfur protein 5 (*ndufs5*), E3 ubiquitin-protein ligase, and microtubule-actin cross-linking factor
169 1. Of these three genes, only *ndufs5* forms a protein complex with mitochondrially encoded
170 proteins, which along with other evidence implicates it as one of the interacting partners in the
171 mitonuclear incompatibility (Fig. 1C; see Supplementary Information 1.1.8 for analysis of other
172 genes).

173 Analysis of three natural hybrid populations that had fixed the mitochondrial haplotype of
174 one of the parental species (Fig. S5) confirmed that this region on chromosome 13 is under
175 selection in natural hybrid populations, with the strongest signal of selection localizing precisely
176 to the same three genes found under the admixture mapping peak (Fig. S6A; Supplementary
177 Information 1.1.6). Moreover, comparing genotypes and phenotypes in siblings allowed us to
178 exclude maternal effects as a driver of the chromosome 13 signal (Supplementary Information
179 1.1.7), and we ruled out the possibility that other confounding factors could generate the
180 observed patterns (Supplementary Information 1.1.9).

181 We also identified a peak on chromosome 6 that approached genome-wide significance
182 (Fig. 1G; Table S2; Supplementary Information 1.1.10) and fell precisely within the segregation

183 distortion region previously mapped in F_2 hybrids (Fig. 1D; Supplementary Information 1.1.1).
184 This peak contained 20 genes including the mitochondrial Complex I gene *ndufa13* (Fig. S7–S8;
185 Methods, Supplementary Information 1.1.10). Depletion of non-mitochondrial parent ancestry at
186 *ndufa13* was unidirectional (Fig. 1F), consistent with selection acting only against the
187 combination of the *X. malinche* mitochondria with homozygous *X. birchmanni* ancestry at
188 *ndufa13* (see Supplementary Information 1.2.3–1.2.4). Genomic analyses in natural hybrid
189 populations confirmed this asymmetry (Fig. S6B).
190 Together, these results indicate that at least two *X. birchmanni* nuclear genes cause
191 incompatibility when they are mismatched in ancestry with the *X. malinche* mitochondria (Fig.
192 1H; Supplementary Information 1.2.5). These genes, *ndufs5* and *ndufa13*, belong to a group of
193 proteins and assembly factors that form respiratory Complex I[51] (see Table S1 for locations of
194 the 51 annotated Complex I genes in the *Xiphophorus* genome). Complex I is the first component
195 of the mitochondrial electron transport chain that ultimately allows the cell to generate ATP.
196 Both nuclear proteins interface with several mitochondrially derived proteins at the core of the
197 Complex I structure, hinting at the possibility that physical interactions could underlie this multi-
198 gene mitonuclear incompatibility.
199
200 **Interactions with the *X. birchmanni* mitochondria**
201
202 Admixture mapping analysis also identified a strong peak of mitonuclear association on
203 chromosome 15, which we briefly discuss here and in Supplementary Information 1.1.10 and
204 1.2.1. This peak was associated with *X. birchmanni* mitochondrial ancestry (Fig. S9), indicating
205 that it has a distinct genetic architecture from the incompatibility involving the *X. malinche*

206 mitochondria and *X. birchmanni ndufs5* and *ndufa13*. Specifically, analysis of genotypes at the
207 admixture mapping peak indicates that the *X. birchmanni* mitochondria is incompatible with
208 homozygous *X. malinche* ancestry on chromosome 15 (Fig. 1C, Fig. S9). This region did not
209 contain any members of Complex I, but dozens of genes in this interval interact with known
210 mitonuclear genes (see Table S3; Supplementary Information 1.1.10). The fact that we detect
211 incompatible interactions with both the *X. malinche* mitochondria (at *ndufs5* and *ndufa13*) and
212 the *X. birchmanni* mitochondria (*ndufs5* and chromosome 15) in our admixture mapping results
213 supports the idea that mitonuclear interactions can act as "hotspots" for the evolution of hybrid
214 incompatibilities[16].
215
216 **Lethal Effect of Incompatibility in Early Development**
217
218 The combination of *X. birchmanni ndufs5* or *ndufa13* with the *X. malinche* mitochondria
219 appears to be lethal by the time individuals reach adulthood. To investigate the developmental
220 timing of the incompatibility, we genotyped pregnant females from the admixture mapping
221 population and recorded the developmental stages of their embryos[52] (swordtails are livebearing
222 fish; see Methods). We found a significant interaction between developmental stage and *ndufs5*
223 genotype, whereas *ndufa13* genotype did not affect developmental stage (Fig. S10–13;
224 Supplementary Information 1.3.1). While developmental asynchrony is typically on the scale of
225 0–2 days in pure species[53] (Supplementary Information 1.3.1), we observed much greater
226 variation in broods collected from the admixture mapping population where the mitochondrial
227 incompatibility is segregating (e.g. stages normally separated by roughly 12 days of development
228 found in the same brood; Supplementary Information 1.3.1; Fig. 2A–B). Genotyping results

229 revealed that embryos with homozygous *X. birchmanni* ancestry at *ndufs5* and *X. malinche*
230 mitochondria are present at early developmental stages, but that these embryos failed to develop
231 beyond a phenotype typical of the first seven days of gestation (the full length of gestation is 21–
232 28 days in *Xiphophorus*; Fig. 2A–B, Fig. 2D–E). Individuals with mismatched ancestry at *ndufs5*
233 whose siblings were fully developed still had a detectable heartbeat but had consumed less yolk
234 than their siblings and remained morphologically underdeveloped (Fig. 2D, Fig. S14–19). Unlike
235 other species, in *Xiphophorus* this developmental lag could itself cause mortality, since embryos
236 that do not complete embryonic development inside the mother fail to survive more than a few
237 days after birth (Supplementary Information 1.3.1; Table S4). Given that Complex I inhibition
238 lethally arrests development in zebrafish embryos[54,55], we also tested the effects of Complex I
239 inhibition on *X. birchmanni* and *X. malinche* fry, and found a similar level of sensitivity
240 (Supplementary Information 1.3.2).
241 In contrast to individuals with mismatched ancestry at *ndufs5,* those with *ndufa13*
242 mismatch survived embryonic development but suffered mortality in the early post-natal period
243 (Fig. 2C). We tracked 74 F_2 fry from 24 hours post-birth through adulthood (Supplementary
244 Information 1.3.3). We found that most fry with incompatible genotypes at *ndufa13* had already
245 suffered mortality by the time tracking began, with only 7 individuals found 24 hours post-birth
246 that were homozygous *X. birchmanni* at *ndufa13* (versus 19 expected; binomial $P = 0.0005$). No
247 natural mortality was observed between 1 day and 3 months post-birth (one individual exhibiting
248 distress was euthanized, and was a *ndufa13* incompatible homozygote; see Supplementary
249 Information 1.3.3).
250
251

252 **Evidence for Complex Physiological and Fitness Effects in Incompatible Individuals**

253

254 Our analysis of developing embryos indicates that individuals with the *ndufs5*
255 incompatibility exhibit delayed or arrested embryonic development, whereas those with the
256 *ndufa13* incompatibility did not. This suggests that these genes may drive lethality through
257 partially distinct mechanisms. As such, we chose to further investigate the effects of *ndufs5* and
258 *ndufa13* and their possible interactions using a paired genotyping and physiological approach
259 throughout development. We sampled 235 F_2 embryos at a range of developmental stages and
260 measured their overall rates of respiration (Supplementary Information 1.3.4–1.3.5). We also
261 used imaging of these embryos to track cardiovascular phenotypes as these have been associated
262 with *ndufa13* defects in mammals[56]. We found that incompatible genotypes at *ndufs5* and
263 *ndufa13* impacted a range of phenotypes, including heart rate, length relative to compatible
264 siblings, and length-corrected head size (Fig. S14–22, Table S5–S7). *ndufa13* mismatch has a
265 large effect on cardiovascular phenotypes, including heart rate and the size of the sinu-atrium (an
266 embryo-specific heart chamber, Fig. 2G–H, Fig. S22, Table S6, S8); *ndufs5* affects only heart
267 rate (Fig. S19, Table S6). We find initial evidence that cardiac defects persist into adulthood in
268 surviving individuals with *ndufa13* mismatch (see Supplementary Information 1.3.3; Fig. S23).
269 By contrast, *ndufs5* mismatch has a major impact on rates of respiration and yolk consumption
270 during development (Fig. 2F, while *ndufa13* only affects respiration through an interaction with
271 *ndufs5* and body length, Fig. S24–27, Table S9–11).

272 Naively, the separable impacts of incompatible genotypes at *ndufs5* and *ndufa13* could
273 indicate that even though these proteins are in physical contact in Complex I (see below), they
274 represent two distinct hybrid incompatibilities. We investigated this question by taking

275 advantage of rare survivors of the *ndufa13* incompatibility in an expanded dataset of 1010 F_2
276 hybrids. Using this dataset, we were able to identify dozens of survivors of the *ndufa13*
277 incompatibility (3.4% of individuals) and found that genotypes at *ndufa13* and *ndufs5* were not
278 independent (χ^2 association test $P = 0.032$, Supplementary Information 1.2.5). Upon further
279 investigation, we found that the majority of survivors of the *ndufa13* incompatibility had
280 homozygous *X. malinche* ancestry at *ndufs5*, suggesting that harboring even one *X. birchmanni*
281 allele at *ndufs5* may sensitize fry to the *ndufa13* incompatibility. Indeed, we found that
282 individuals that had heterozygous ancestry at *ndufs5* were significantly under-represented among
283 surviving *ndufa13* incompatible individuals (Permutation test $P = 0.015$, Fig. 2I, Supplementary
284 Information 1.2.5). These findings highlight a subtle but significant non-additive effect of *ndufs5*
285 and *ndufa13* on survival.
286
287 **Mitochondrial Biology in Adult Hybrids Heterozygous for the Incompatibility**
288
289 Because few individuals homozygous for incompatible genotypes at *ndufs5* or *ndufa13*
290 survive past birth, our previous experiments focused on embryos. However, the small size of
291 *Xiphophorus* embryos prevents us from using assays that directly target Complex I. To further
292 explore the effects of the hybrid incompatibility on Complex I function *in vivo*, we turned to
293 adult F_1 hybrids between *X. birchmanni* and *X. malinche* (Fig. 3A). Since F_1 hybrids that derive
294 their mitochondria from *X. malinche* and are heterozygous for ancestry at *ndufs5* and *ndufa13* are
295 fully viable, we asked whether there was evidence for compensatory nuclear or mitochondrial
296 regulation that might be protective in F_1 hybrids. We found no evidence for significant
297 differences in expression of *ndufs5* or *ndufa13* (Supplementary Information 1.3.6; Fig. S28–29)

298 or in mitochondrial copy number (Supplementary Information 1.3.7; Fig. 3B) between F_1 hybrids
299 and parental species.

300 With no indication of a compensatory regulatory response, we reasoned that we might be
301 able to detect reduced mitochondrial Complex I function in hybrids heterozygous for ancestry at
302 *ndufs5* and *ndufa13.* We quantified respiratory phenotypes in isolated mitochondria using an
303 Oroboros O2K respirometer in adult hybrids and both parental species (Fig. S30; Methods,
304 Supplementary Information 1.3.8). We found that Complex I efficiency was lower in hybrids
305 compared to the two parental species (Fig. 3C, Fig. S31, orthogonal contrast $t = -2.53$, $P = 0.023$,
306 n = 7 per genotype), and that the time required for hybrids to reach maximum Complex I-driven
307 respiration was ~2.5 times longer (orthogonal contrast $t = 4.303$, $P < 0.001$; Fig. 3D; Fig. S32).
308 On the other hand, overall levels of mitochondrial respiration were unaffected by genotype (Fig.
309 3E, orthogonal contrast $t = 0.078$, $P = 0.94$, n = 7 per genotype; Supplementary Information
310 1.3.8) as were multiple independent measures of mitochondrial integrity and function (Fig. S31–
311 34, Supplementary Information 1.3.8–1.3.9). Together, these data point to reduced function of
312 Complex I without broader phenotypic consequences in individuals heterozygous for
313 incompatible alleles, as previously observed in other models of Complex I dysfunction[57,58].

314 Given physiological evidence for some reduction in Complex I function in hybrids
315 heterozygous at *ndufs5* and *ndufa13*, we predicted that there might be an altered frequency of
316 protein complexes incorporating both *X. malinche* mitochondrial proteins and *X. birchmanni*
317 proteins at *ndufs5* and *ndufa13* in F_1 hybrids. To test this prediction, we took a mass
318 spectrometry-based quantitative proteomics approach. We used stable isotope-labeled peptides to
319 distinguish between the *X. birchmanni* and *X. malinche ndufs5* and *ndufa13* peptides in
320 mitochondrial proteomes extracted from F_1 hybrids (n = 5, see Methods, Supplementary

321 Information 1.4.1–1.4.4). While endogenous *ndufa13* peptides were not observed frequently
322 enough to quantify accurately, we found consistent deviations from the expected 50-50 ratio of
323 *X. birchmanni* to *X. malinche* peptides for *ndufs5* in F_1 hybrids, with a significant
324 overrepresentation of matched ancestry at *ndufs5* in the mitochondrial proteome ($t = 3.96$, $P =$
325 0.016; Fig. 3F; Fig. S35; Supplementary Information 1.4.5). Since we did not observe allele-
326 specific expression of *ndufs5* (Fig 3F; Supplementary Information 1.3.6), this result is consistent
327 with disproportionate degradation of *X. birchmanni*-derived *ndufs5* peptides in the mitochondrial
328 proteome or differences in translation of *ndufs5* transcripts derived from the two species.
329
330 **Paired mitonuclear substitutions at contact sites in Complex I**
331
332 While we can leverage high resolution admixture mapping to pinpoint the nuclear
333 components of the hybrid incompatibility, we cannot take this approach to distinguish among the
334 37 genes in the swordtail mitochondrial genome because they do not undergo meiotic
335 recombination. To begin to explore the possible mitochondrial partners of *ndufs5* and *ndufa13*,
336 we therefore turned to protein modeling, relying on high quality cryo-EM based structures[59–61].
337 Although these structures are only available for distant relatives of swordtails, the presence of
338 the same set of supernumerary Complex I subunits and high sequence similarity suggest that
339 using these structures is appropriate (Table S12–S13; Fig. S36–S38; Supplementary Information
340 1.4.6).
341 Barring a hybrid incompatibility generated by regulatory divergence (see Supplementary
342 Information 1.3.6), our expectation is that hybrid incompatibilities will be driven by amino acid
343 changes in interacting proteins[62]. We used the program RaptorX[63] to generate predicted

344 structures of *X. birchmanni* and *X. malinche ndufs5, ndufa13*, and nearby Complex I
345 mitochondrial and nuclear genes, which we aligned to a mouse cryo-EM Complex I structure[59]
346 (Fig. 4A; Fig. S36–S38; Methods). Using these structures, we visualized amino acid substitutions
347 between *X. birchmanni* and *X. malinche* at the interfaces of *ndufs5, ndufa13* and mitochondrially
348 encoded genes (Fig. S39–S41). While there are dozens of substitutions in the four
349 mitochondrially encoded genes that are in close physical proximity to *ndufs5* or *ndufa13* (Fig.
350 S36; *nd2, nd3, nd4l,* and *nd6*), there are only five cases where amino acid substitutions in either
351 nuclear gene are predicted to be close enough to contact substitutions in any mitochondrial gene,
352 all of which involve *nd2* or *nd6* (Table S14, Fig. 4A; see Fig. S40 for pairwise visualizations of
353 interacting proteins). These paired substitutions in regions of close proximity between
354 mitochondrial- and nuclear-encoded proteins suggest that *nd2* and *nd6* are the genes most likely
355 to be involved in the mitochondrial component of the hybrid incompatibility (Fig. 4A–B; Fig.
356 S41–S44). While there are currently no developed approaches for transgenics in livebearing fish
357 like *Xiphophorus* (Supplementary Information 1.3.1) and Complex I is ill-suited for *in vitro*
358 approaches (being comprised of 45 subunits with an intricate assembly process[64]), manipulating
359 these in-contact substitutions is an exciting direction for future work.
360
361 **Rapid evolution of Complex I proteins**
362
363 Theory predicts that hybrid incompatibilities are more likely to arise in rapidly evolving
364 genes[4,5,7,15]. Consistent with this hypothesis, *ndufs5* is among the most rapidly evolving genes
365 genome-wide between *X. birchmanni* and *X. malinche* (Fig. 4C–D). Aligning the *ndufs5* coding
366 sequences of *X. birchmanni, X. malinche*, and twelve other swordtail species revealed that all

367 four amino acid substitutions that differentiate *X. birchmanni* and *X. malinche* at *ndufs5* were
368 derived on the *X. birchmanni* branch (Fig. 4C). Phylogenetic tests indicate that there has been
369 accelerated evolution of *ndufs5* on this branch ($d_N/d_S > 99$, N = 4, S = 0, codeml branch test P =
370 0.005, Fig. 4C). Similar patterns of rapid evolution are observed at *ndufa13*, which also showed
371 evidence for accelerated evolution in *X. birchmanni* (Fig. 4E; $d_N/d_S = 1.2$, N = 3, S = 1, codeml
372 branch test $P = 0.002$). While explicit tests for adaptive evolution at *ndufs5* and *ndufa13* could
373 not exclude a scenario of relaxed selection (Supplementary Information 1.5.1, 1.5.2), our
374 comparisons across phylogenetic scales highlight strong conservation in some regions of the
375 proteins and rapid turnover in others, complicating our interpretation of this test (Fig. S45).
376 Rapid evolution of *ndufs5* and *ndufa13* could be driven by coevolution with
377 mitochondrial substitutions, a mechanism that has been proposed to explain the outsized role of
378 the mitochondria in hybrid incompatibilities[16,65]. Indeed, there is an excess of derived
379 substitutions in the *X. birchmanni* mitochondrial protein *nd6*, one of the proteins that physically
380 contacts *ndufs5* and *ndufa13* (Table S15; Fig. S42; codeml branch test $P = 0.005$). Moreover,
381 several of the substitutions observed in both mitochondrial and nuclear genes are predicted to
382 have functional consequences (Supplementary Information 1.5.1; Table S16), including ones
383 predicted to be in contact between *ndufs5, ndufa13, nd2*, and *nd6* (Fig. 4A, 4B; Fig. S41).
384

385 **Introgression of genes underlying mitonuclear incompatibility**

386 The presence of a mitonuclear incompatibility in *Xiphophorus* is especially intriguing,
387 given previous reports that mitochondrial genomes may have introgressed between species[37].
388 While *X. malinche* and *X. birchmanni* are sister species based on the nuclear genome, they are
389 mitochondrially divergent, with *X. malinche* and *X. cortezi* grouped as sister species based on the

390 mitochondrial phylogeny[37] (Fig. 5A–B). As we show, all *X. cortezi* mitochondria sequenced to
391 date are nested within *X. malinche* mitochondrial diversity (Fig. 5B, Fig. S42, S46;
392 Supplementary Information 1.5.3–1.5.4). Simulations indicate that gene flow, rather than
393 incomplete lineage sorting, drove replacement of the *X. cortezi* mitochondria with the *X.*
394 *malinche* sequence ($P < 0.002$ by simulation; Fig. 5C; Supplementary Information 1.5.4).
395 The introgression of the mitochondrial genome from *X. malinche* into *X. cortezi* raises the
396 possibility that other Complex I genes may have co-introgressed[66]. Indeed, the nucleotide
397 sequence for *ndufs5* is identical between *X. malinche* and *X. cortezi*, and the sequence of *ndufa13*
398 differs by a single synonymous mutation (although conservation of both genes is high throughout
399 *Xiphophorus*; Fig. S47–S48). These identical amino acid sequences suggest that hybrids between
400 *X. cortezi* and *X. birchmanni* are likely to harbor the same mitonuclear incompatibility we
401 observe between *X. malinche* and *X. birchmanni*, as a result of ancient introgression between *X.*
402 *malinche* and *X. cortezi* (Fig. 5D; Supplementary Information 1.5.3–1.5.5).
403 This inference is supported by analysis of ancestry in three contemporary *X. birchmanni*
404 × *X. cortezi* hybrid populations[48], two of which are completely geographically isolated,
405 indicating that the hybridization events were independent (Fig. S49). We find that all known *X.*
406 *birchmanni* × *X. cortezi* hybrid populations are fixed for the mitochondrial genome from *X.*
407 *cortezi* (that originated in *X. malinche*) and also show a striking depletion of non-mitochondrial
408 parent ancestry at *ndufs5* and *ndufa13* (Fig. 5E; Fig. S50; Supplementary Information 1.5.6).
409 This repeated depletion is not expected by chance (Fig. 5E; Supplementary Information 1.5.6, P
410 $= 0.0001$ by simulation) and instead indicates that selection has removed mismatched ancestry in
411 these regions of the genome. These results suggest that the mitonuclear incompatibility observed
412 in *X. birchmanni* × *X. malinche* is also active in hybridizing *X. birchmanni* × *X. cortezi*

413 populations. This exciting finding shows for the first time that genes underlying hybrid

414 incompatibilities can introgress together, transferring incompatibilities between related species.

415 ## Discussion

416 What genetic and evolutionary forces drive the emergence of hybrid incompatibilities,
417 especially between closely related species? Theory predicts that hybrid incompatibilities
418 involving multiple genes should be common[6,7], but with few exceptions[8,11–13], they remain
419 virtually uncharacterized at the genic level[6]. Here, we identify incompatible interactions in
420 mitochondrial Complex I that causes hybrid lethality in lab and wild populations. Our findings in
421 naturally hybridizing species echoes predictions from theory and studies in lab models[8,11–13] that
422 protein complexes may be a critical site of hybrid breakdown.

423 Researchers have proposed mitonuclear interactions as "hotspots" for the emergence of
424 hybrid incompatibilities, given that mitochondrial genomes often experience higher substitution
425 rates between species[18–20], yet must intimately interact with nuclear proteins to perform essential
426 cellular functions[25,26]. Our findings support this prediction, identifying incompatible interactions
427 with both the *X. malinche* and *X. birchmanni* mitochondria. We also show that there has been
428 exceptionally rapid evolution in both mitochondrial and interacting nuclear genes in *X.*
429 *birchmanni*, which we speculate may have introduced mutations that are incompatible in hybrids
430 (Fig. 4). Whether driven by adaptation or some other mechanism, our findings support the
431 hypothesis that the coevolution of mitochondrial and nuclear genes could drive the
432 overrepresentation of mitonuclear interactions in hybrid incompatibilities[25,26,65]. More broadly,
433 our results are consistent with predictions that rapidly evolving proteins are more likely to
434 become involved in hybrid incompatibilities than their slowly evolving counterparts[4,5,15].

435 Characterizing the incompatibility across multiple scales of organization allowed us to
436 explore the mechanisms through which it acts[67–69]. Our results suggest that in the case of the *X.*
437 *malinche* mitochondria hybrid lethality is mediated through arrested development *in utero* of

438 individuals with mismatched ancestry at *ndufs5*, while individuals with *ndufa13* mismatch have
439 vascular defects and typically die shortly after birth. Intriguingly, individuals with *ndufa13*
440 mismatch that do survive are much less likely to harbor any *X. birchmanni* alleles at *ndufs5*
441 (even in the heterozygous state; Fig. 2I). Taken together, our results indicate that a subtle three-
442 way interaction overlays two strong pairwise mitonuclear incompatibilities at *ndufs5* and
443 *ndufa13*. Evolutionary biologists have been fascinated by the idea that hybrid incompatibilities
444 may commonly involve three or more genes following theoretical work by Orr[7] almost thirty
445 years ago, but this question has been challenging to address empirically. Our results highlight
446 how the nuances of actual fitness landscapes may defy simplifying assumptions.
447 Finally, this mitonuclear incompatibility provides a new case in which the same genes are
448 involved in incompatibilities across multiple species[38,46,70]. However, tracing the evolutionary
449 history of the genes that underlie it adds further complexity to this phenomenon: we found that
450 introgression has resulted in the transfer of genes underlying the incompatibility from *X.*
451 *malinche* to *X. cortezi*, and evidence from *X. birchmanni* × *X. cortezi* hybrid populations
452 indicates that the incompatibility is likely under selection in these populations as well. The
453 possibility that hybridization could transfer incompatibilities between species has not been
454 previously recognized, perhaps due to an underappreciation of the frequency of hybridization.
455 The impact of past hybridization on the structure of present-day reproductive barriers between
456 species is an exciting area for future inquiry.
457
458

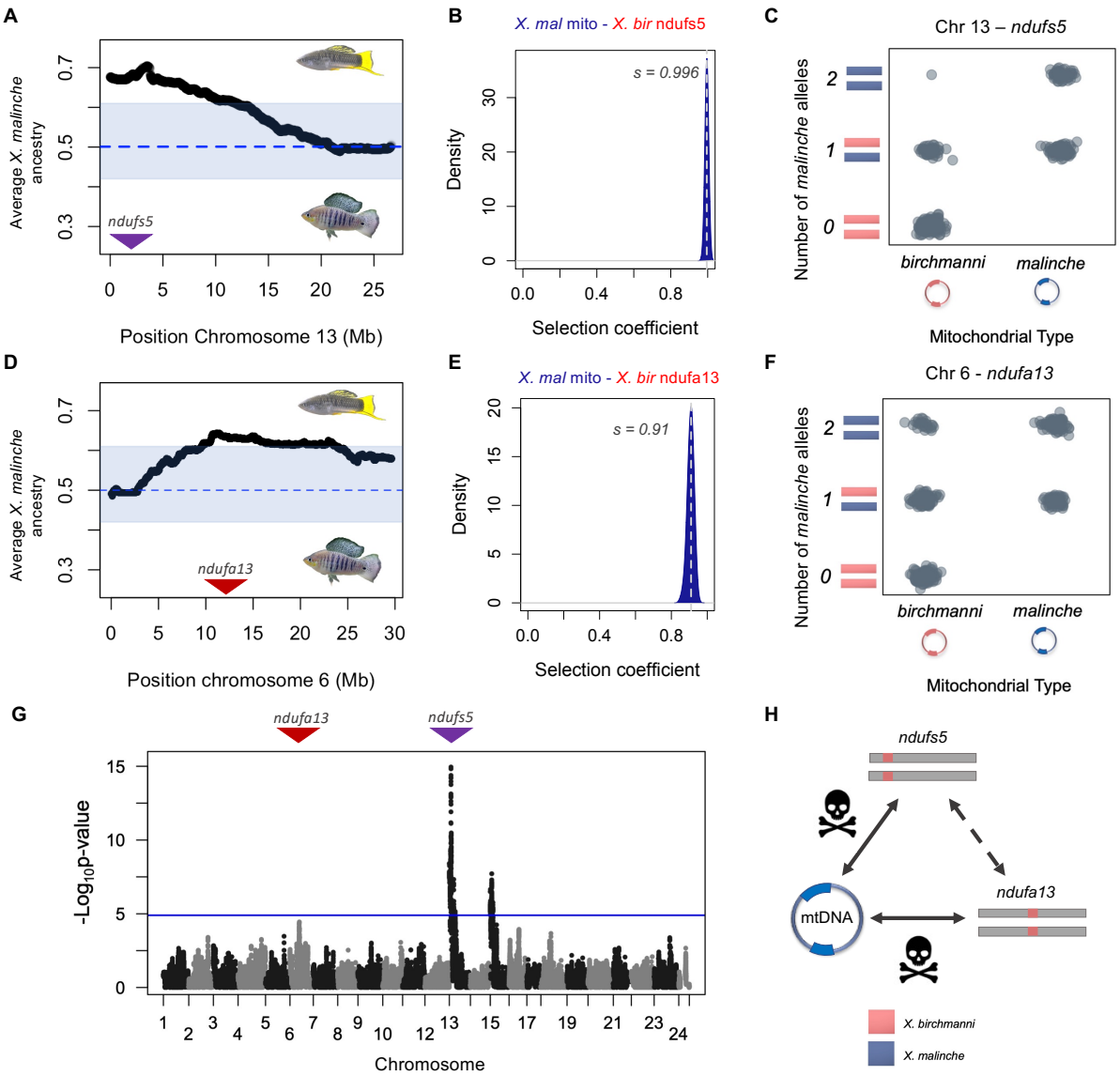

Fig. 1 | Admixture mapping pinpoints mitonuclear incompatibility in *Xiphophorus*. (**A**) Average ancestry of F_2 hybrids on chromosome 13 reveals segregation distortion towards *X. malinche* ancestry across a large region of the chromosome. Blue envelope shows the 99% quantiles of *X. malinche* ancestry at all ancestry informative sites genome wide. Dashed line represents the expected *X. malinche* ancestry for this cross. Purple arrow points to the position of *ndufs5*. (**B**) Results of approximate Bayesian computation (ABC) simulations estimating the strength of selection on the *X. malinche* mitochondria when combined with *X. birchmanni* ancestry at *ndufs5*. Shown here is the posterior distribution from accepted simulations; vertical line and inset indicates the maximum a posteriori estimate for the selection

468 coefficient. (**C**) Observed genotype frequencies of different genotype combinations of *ndufs5*
469 (chromosome 13) and mitochondrial haplotypes in the admixture mapping population. (**D**) Average
470 ancestry of F_2s on chromosome 6, reveals segregation distortion towards *X. malinche* ancestry across a
471 large region of the chromosome. Blue envelope and dashed line indicate 99% ancestry quantiles and
472 expected ancestry in the cross as in (**A**), red arrow points to the position of *ndufa13*. (**E)** Results of
473 approximate Bayesian computation (ABC) simulations estimating the strength of selection on the
474 combination of *X. malinche* mitochondria with *X. birchmanni ndufa13*, as in (**B**). (**F**) Observed genotype
475 frequencies of different genotype combinations of *ndufa13* (chromosome 6) and mitochondrial haplotypes
476 in the admixture mapping population. (**G**) Admixture mapping results for associations between nuclear
477 ancestry and mitochondrial haplotype in natural hybrids, controlling for genome-wide ancestry. Blue line
478 indicates the 10% false positive rate genome-wide significance threshold determined by simulations. The
479 peak visible on chromosome 15 is driven by interactions with the *X. birchmanni* mitochondria and an
480 unknown nuclear gene and is discussed in Supplementary Information 1.1.10 and 1.2.1. (**H**) Schematic of
481 identified interactions with the *X. malinche* mitochondrial genome from our mapping data. We detect a
482 subtle interaction between *ndufs5* and *ndufa13* (indicated by the dashed line; see main text, Figure 2, and
483 Supplementary Information 1.2.5).

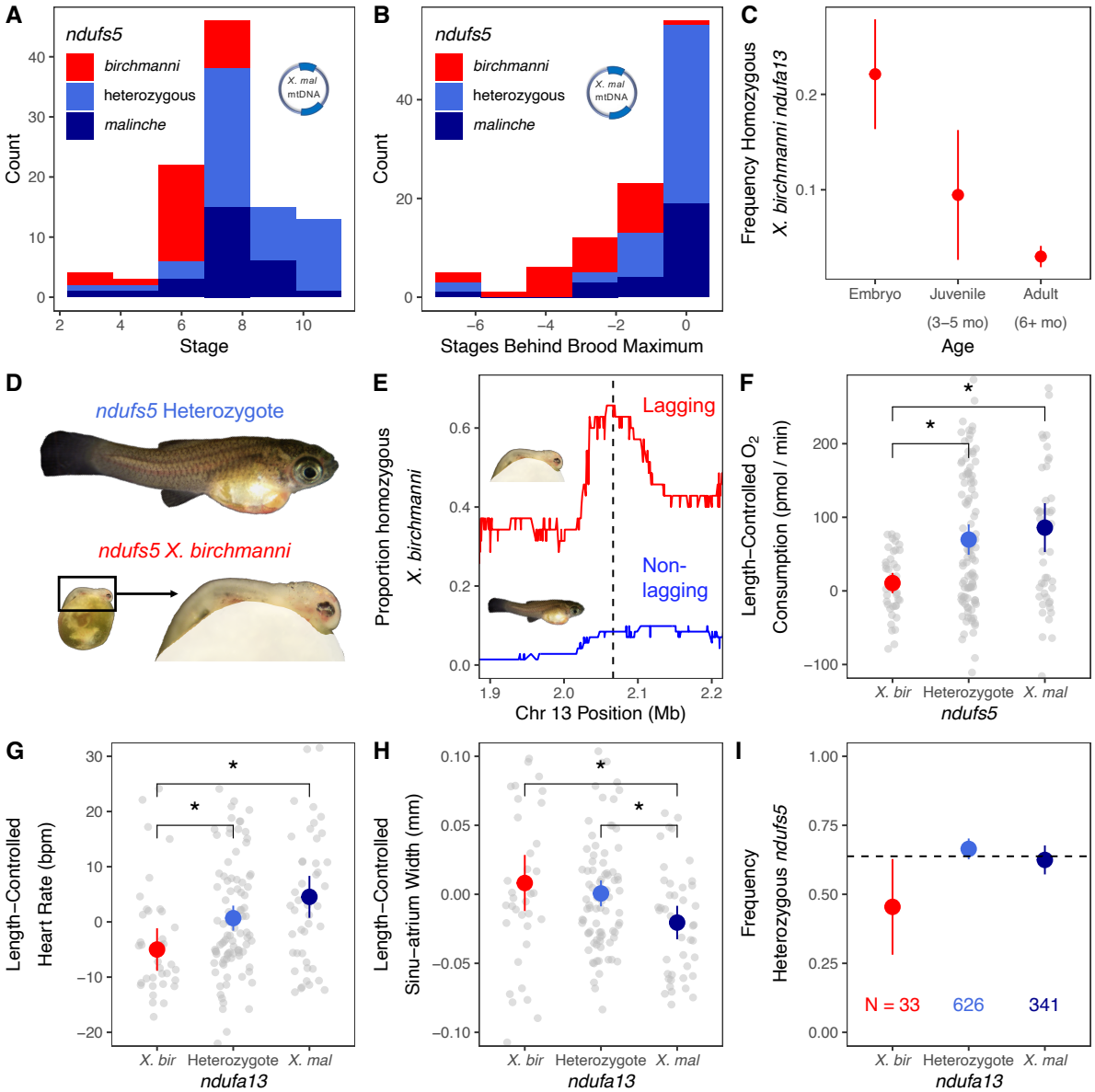

Fig. 2 | Impact of the hybrid incompatibility on *Xiphophorus* hybrid embryos. (**A**) Developmental stage and *ndufs5* genotypes of hybrid embryos with *X. malinche* mitochondria. **(B)** Lag in development of hybrid embryos with *X. malinche* mitochondria compared to the most developed embryo in their brood, as a function of *ndufs5* genotype. (**C**) Change in frequency of homozygous *X. birchmanni* ancestry at *ndufa13* in F_2 hybrids over development. Points and lines represent the estimate ± 2 standard errors, based on observed frequency and sample size. (**D**) F_2 hybrid siblings showing stark difference in developmental progression as a function of *ndufs5* genotype. Top photo shows entire length of heterozygote embryo,

492 while bottom photos show lagging *ndufs5*-incompatible sibling at matched scale (left) and zoomed for
493 detail (right). (**E**) Frequency of homozygous *X. birchmanni* ancestry along chromosome 13 in embryos
494 with *X. malinche* mitochondria that lagged their siblings in developmental stage by ≥1 developmental
495 stage (red) versus frequency of homozygous *X. birchmanni* ancestry in embryos that did not exhibit
496 developmental lag (blue, see Supplementary Information 1.1.7). Dashed line indicates the location of
497 *ndufs5*. Note that only 66% of embryos with developmental lag have homozygous *X. birchmanni* in this
498 region, indicating that there are other causes of this phenotype. For the same analysis of chromosomes 6
499 and 15, where we see no clear difference in average ancestry as a function of lag status, see Fig. S11–13.
500 (**F–H**) Respiratory and morphometric measurements in live F_2 embryos. To control for the effect of
501 length on other variables, residuals of each variable regressed against body length are plotted (see
502 Supplementary Information 1.3.4-1.3.5). Gray points denote individual measurements, colored points and
503 bars show mean ± 2 SE for each genotype, and brackets with asterisks denote significant differences
504 based on a Tukey's HSD test. (**F**) Relationship between *ndufs5* genotype and respiration in F_2 hybrid
505 embryos, as measured by Loligo plate respirometer. (**G**) Relationship between *ndufa13* genotype and
506 heart rate in F_2 hybrid embryos. (**H**) Relationship between *ndufa13* genotype and the width of the sinu-
507 atrium, which peristaltically pumps blood from the yolk into the embryonic heart atrium. (**I**) Frequency of
508 individuals heterozygous for ancestry at *ndufs5* (i.e. those with one *X. birchmanni* allele) among juveniles
509 and adults of varying *ndufa13* genotypes. Points and lines represent observed frequency ± 2 standard
510 errors. Dashed line represents expected frequency of *ndufs5* heterozygotes under a scenario of additive
511 selection on *ndufs5* and *ndufa13* (see Supplementary Information 1.2.5).

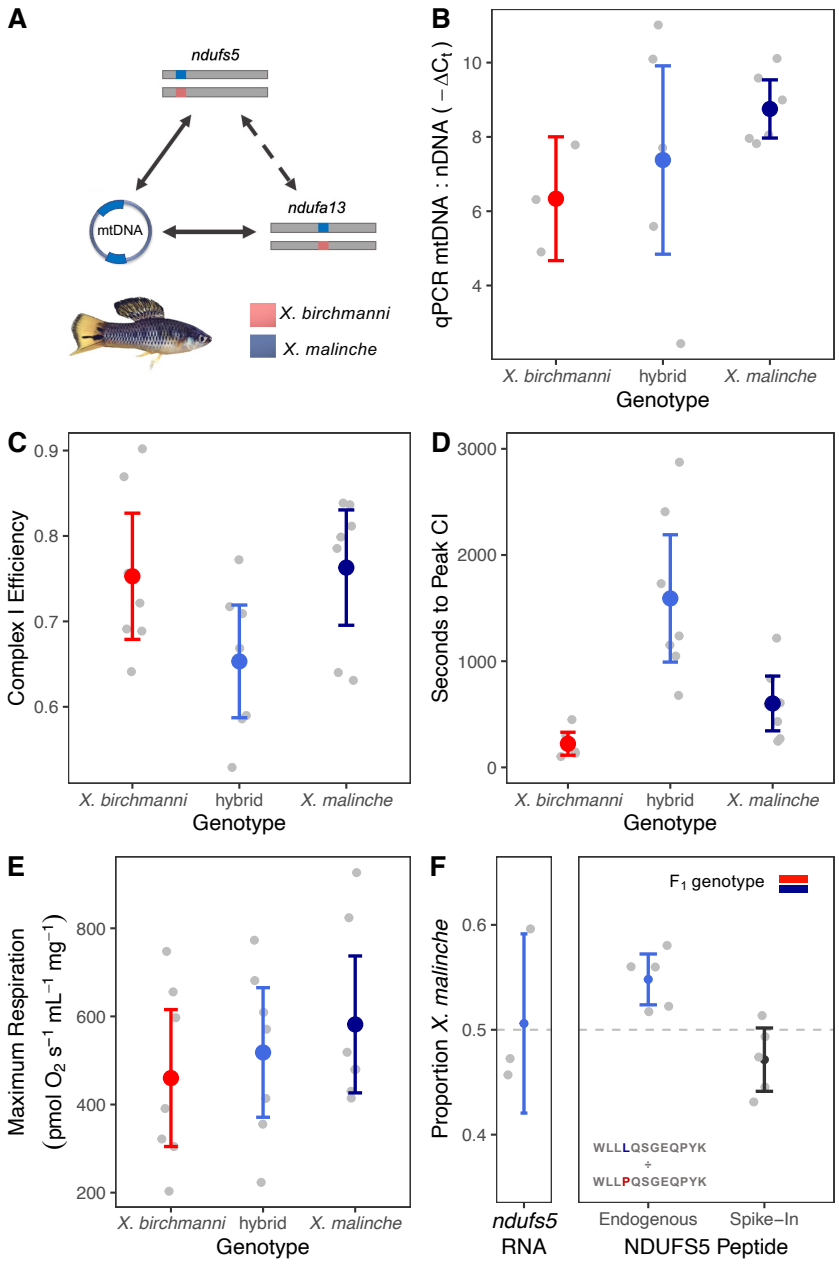

Fig. 3 | Physiological and proteomic phenotypes of viable heterozygotes harboring the hybrid incompatibility. In all panels, colored points and whiskers show the mean ± 2 standard errors, and gray points show individual data. (**A**) Schematic of ancestry at loci involved in the incompatibility in an *X. birchmanni* × *malinche* F_1 hybrid. Hybrids heterozygous at both loci avoid the lethal effects of the interaction between the *X. malinche* mitochondria and *X. birchmanni* ancestry at *ndufs5* and *ndufa13* (Supplementary Information 1.2.2). (**B**) Results of rt-qPCR evaluating evidence for differences in mitochondrial copy number between genotypes in liver tissue. Ratio is derived from the difference in C_t

between a single copy nuclear gene (*Nup43*) and the mitochondrial gene *ND1*. (**C**) Results of Oroboros O2K respirometer assay for adult *X. birchmanni*, *X. malinche*, and hybrid individuals with *X. malinche* mitochondria and heterozygous ancestry at *ndufs5* and *ndufa13* (n=7 per genotype) point to lower Complex I efficiency in heterozygous hybrids (orthogonal contrast $P = 0.023$). (**D**) Time to reach the maximum rate of Complex I-driven respiration after the addition of ADP differed between heterozygous hybrids and parental species (orthogonal contrast $P < 0.001$). Complex I-driven respiration begins with the addition of ADP, as the flow of electrons is previously limited by the inability of Complex V to relieve the proton gradient in the absence of its substrate (see Fig. S32 for example time-to-peak curves). Time to reach the peak in Complex I- and Complex II-driven respiration after the addition of succinate did not differ across genotypes (Fig. S33). (**E**) Maximum respiration rates during full O2K protocol as a function of genotype did not differ between groups despite significant differences in Complex I efficiency in heterozygotes (orthogonal contrast $P = 0.94$). (**F**) Allelic balance of *ndufs5* in the F_1 hybrid proteome and transcriptome. Left subplot shows allele-specific expression of *ndufs5* in three adult F_1 hybrids. Right subplot shows results of quantitative mass spectrometry analysis of *ndufs5* peptides in mitochondrial proteomes derived from five adult F_1 hybrids. Data points show the proportion of area under the spectral curves contributed by the *X. malinche* allele in a given individual. Left column shows results for endogenous peptides present in F_1 hybrids, and right column shows results for the control where heavy-labeled standards of each peptide were spiked in. Inset shows the identities of heavy-labeled peptides for each species.

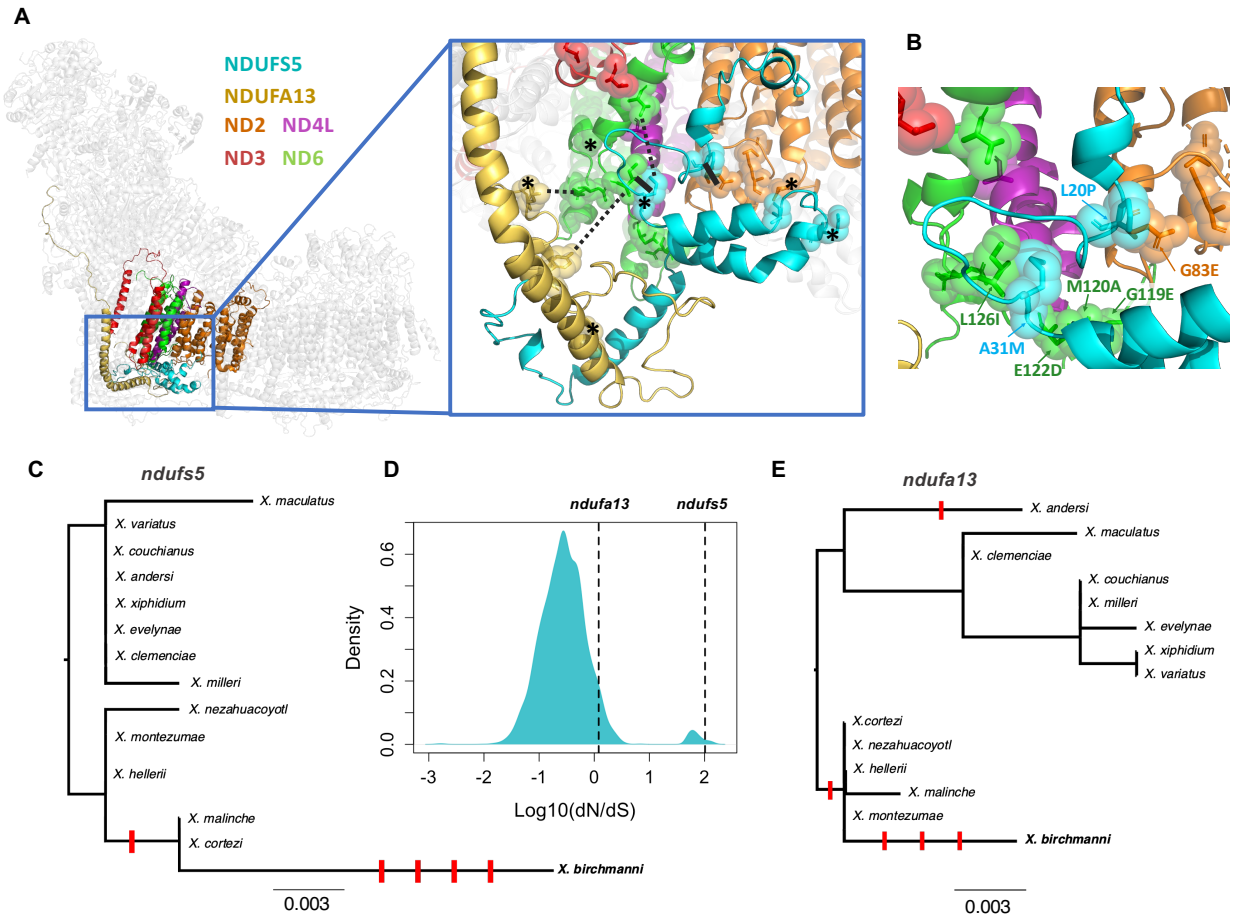

Fig. 4 | Predicted structures of *Xiphophorus* respiratory Complex I and evolutionary rates of incompatible alleles. (**A**) *Xiphophorus* respiratory Complex I structures generated by RaptorX using alignment to a template mouse cryo-EM structure. Colored protein structures include *ndufs5, ndufa13*, and the four mitochondrially encoded *nd* genes in contact with *ndufs5* or *ndufa13*. Inset shows the surface of predicted contacts between these genes. Solid black lines highlight two areas predicted to be in close contact between interspecific substitutions (alpha carbon distance ≤ 10 Angstrom for all models), while dashed lines show three additional areas in which there was weaker evidence for a predicted contact based on computational analyses (side chain distance ≤ 12 Angstrom in at least one model). Asterisks denote residues with substitutions in *X. birchmanni* computationally predicted to affect protein function (Table S16). (**B**) Detailed view of interface between *ndufs5*, *nd2*, and *nd6.* Spheres highlight substitutions between *X. birchmanni* and *X. malinche*. For substitutions predicted to be in close proximity, residues are

552 labeled with letters denoting the *X. malinche* allele, the residue number, and the *X. birchmanni* allele,
553 respectively (see Supplementary Information 1.4.6 and Table S16 for details). (**C**) Gene tree for *ndufs5*
554 generated with RAxML, highlighting an excess of substitutions along the *X. birchmanni* branch. Scale bar
555 represents number of nucleotide substitutions per site. Derived non-synonymous substitutions are
556 indicated by red ticks along the phylogeny. Note that spacing between ticks is arbitrary. (**D**) Distribution
557 of $\mathrm{Log}_{10}\ d_N/d_S$ between *X. birchmanni* and *X. malinche* across all nuclear genes in the genome with values
558 for *ndufs5* and *ndufa13* highlighted. (**E**) Gene tree for *ndufa13* generated with RAxML, highlighting an
559 excess of substitutions along the *X. birchmanni* branch (as in C).
560
561

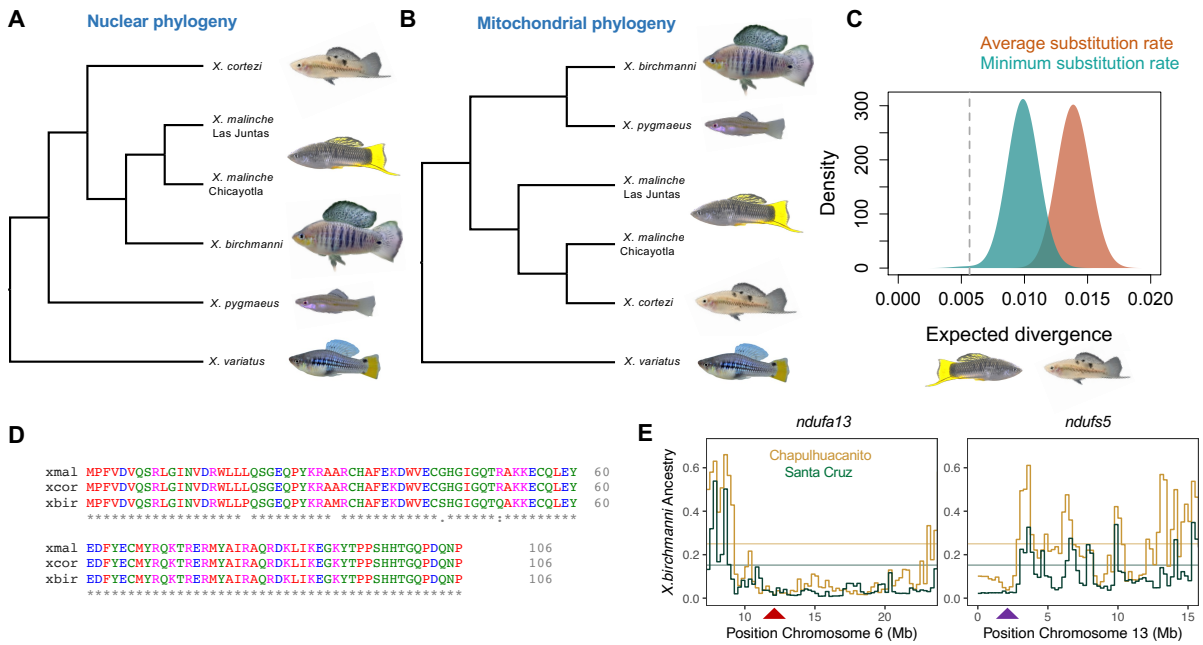

Fig. 5 | Phylogenetic analysis and ancestry mapping suggest that genes underlying the mitonuclear incompatibility have introgressed from *X. malinche* into *X. cortezi*. (**A**) Nuclear phylogeny of *Xiphophorus* species, showing that *X. birchmanni* and *X. malinche* are sister species[37]. (**B**) Phylogeny constructed from whole mitochondrial genome sequences showing that *X. cortezi* mitochondria are nested within *X. malinche* mitochondrial diversity. (**C**) Results of simulations modeling expected mitochondrial divergence between *X. malinche* and *X. cortezi* in a scenario with no gene flow. Distributions represent pairwise sequence divergence in two sets of simulations. The first set used the average mitochondrial substitution rate observed between *Xiphophorus* species (red), and the second used the minimum mitochondrial substitution rate observed (blue). The dotted line shows observed divergence between mitochondrial haplotypes in *X. malinche* and *X. cortezi*, indicating that past mitochondrial introgression is more consistent with the observed data than incomplete lineage sorting (Supplementary Information 1.5.4). (**D**) Clustal alignment of *ndufs5* sequences shows that *X. malinche* and *X. cortezi* have identical amino acid sequences at *ndufs5*, hinting at possible introgression of this nuclear gene, while *X. birchmanni* is separated from them by four substitutions. Similar patterns are observed for *ndufa13*. Colors indicate properties of the amino acid, asterisks indicate locations where the amino acid sequences are identical. (**E**) Non-mitochondrial parent ancestry is strongly depleted in natural *X. cortezi* × *X.*

579 *birchmanni* hybrid populations fixed for the *X. cortezi* mitochondrial haplotype (Fig. S50) at *ndufs5* and
580 *ndufa13*. Arrows show the locations of *ndufa13* and *ndufs5* on chromosome 6 and chromosome 13
581 respectively, which fall in the center of minor parent ancestry deserts in both independently formed
582 populations, as expected for strong hybrid incompatibilities. Step curves show average *X. birchmanni*
583 ancestry in 250 kb windows, and horizontal lines show the genome-wide average for each population.
584

585 # Methods

586 **Biological Materials**

587 Wild parental and hybrid individuals used in this study were collected from natural
588 populations in Hidalgo, Mexico (Permit No. PPF/DGOPA-002/19). Artificial F_1 and F_2 hybrids
589 were generated using mesocosm tanks as described previously[47]. Caudal fin clips were used as
590 the source for all DNA isolation and for flow cytometry, and liver tissue for RNAseq,
591 respirometry, and proteomic assays were collected following Stanford APLAC protocol #33071.
592

593 **Genotyping and local ancestry calling**

594 Genomic DNA was extracted from fin clips and individually barcoded tagmentation
595 based libraries were generated (Supplementary Information 1.1.3). Hybrids were genotyped with
596 low-coverage whole genome sequencing followed by local ancestry inference across the 24
597 *Xiphophorus* chromosomes and the mitochondrial genome using the *ancestryinfer*
598 pipeline[46,47,50,71] (Supplementary Information 1.1.3–1.1.4). We converted posterior probabilities
599 for each ancestry state to hard-calls for downstream analysis, using a posterior probability
600 threshold of 0.9, and analyzed ancestry variation across the genome.
601

602 **QTL and admixture mapping**

603 The regions interacting with the mitochondrial genome were first identified based on
604 analysis of segregation distortion in 943 F_2 hybrids generated from F_1 crosses between *X.*
605 *malinche* females and *X. birchmanni* males (Supplementary Information 1.1.1 and Langdon et
606 al[48]). Since all hybrids in this artificial cross harbored the *X. malinche* mitochondria, we scanned
607 for regions of exceptionally high *X. malinche* ancestry along the genome (>60% *X. malinche*

608 ancestry), identifying one such region on chromosome 13 and one on chromosome 6 (Fig. 1; see
609 also[48]). Evidence for interactions between these regions and the mitochondrial genome were
610 confirmed using admixture mapping in two hybrid populations that segregated for the
611 mitochondrial haplotype of both species (Supplementary Information 1.1.2): the Calnali Low
612 hybrid population (N = 359) and the Chahuaco falls hybrid population (N = 244). Briefly, we
613 used a partial correlation analysis to identify regions of the genome strongly associated with
614 mitochondrial ancestry, after regressing out genome-wide ancestry to account for covariance in
615 ancestry due to population structure (see [44] and Supplementary Information 1.1.5, 1.1.9).
616 Significance thresholds were determined using simulations (Supplementary Information 1.1.5;
617 see also Supplementary Information 1.1.6).
618
619 **Estimates of selection on the mitonuclear incompatibility**
620 We used an ABC approach to estimate the strength of selection against the incompatible
621 interaction between the *X. malinche* mitochondrial haplotype and *X. birchmanni* ancestry at the
622 two nuclear genes involved in the hybrid incompatibility: *ndufs5* and *ndufa13* (Supplementary
623 Information 1.2.2). For these simulations, we asked what selection coefficients (0–1) and
624 dominance coefficients (0–1) could generate the observed deviations from the expectation of 50–
625 50 *birchmanni–malinche* ancestry in F_2 hybrids at *ndufs5* and *ndufa13* after two generations of
626 selection. We performed 500,000 simulations for each interaction and accepted or rejected
627 simulations based on comparisons to the real data using a 5% tolerance threshold
628 (Supplementary Information 1.2.2). We also evaluated evidence for incompatible interactions
629 with the *X. birchmanni* mitochondrial haplotype (Supplementary Information 1.2.1–1.2.4).
630

631 **Developmental staging and genotyping of embryos**

632 To pinpoint when in development the incompatibility between the *X. malinche*
633 mitochondria and *X. birchmanni* nuclear genotypes causes lethality, we collected a dataset on the
634 developmental stages of embryos with different genotype combinations. Whole ovaries were
635 removed from pregnant females and embryos were individually dissected. Each embryo was
636 assigned a developmental stage ranging from 1–11 based on established protocols for poeciliid
637 embryos[52]. Unfertilized eggs were excluded from analysis. Following staging, individual
638 embryos (N = 296) were genotyped as described above and in Supplementary Information 1.3.1.
639 We tested for significant differences in developmental stage between siblings with compatible
640 and incompatible genotype combinations using a two-sided two-sample t-test (Supplementary
641 Information 1.3.1) and examined differences in ancestry between large groups of siblings that
642 varied in their developmental stages (Supplementary Information 1.1.7). We also collected data
643 on embryonic stage and variability between siblings in embryonic stage from both pure parental
644 species (Supplementary Information 1.3.1). We used a different approach to pin-point the timing
645 of *ndufa13* lethality given that it appeared to act postnatally (Supplementary Information 1.3.3).
646

647 **Embryo Respirometery and Morphometrics**

648 To study the mechanisms of *ndufs5*- and *ndufa13*-driven lethality, we performed oxygen
649 consumption measurements on F_2 embryos in a Loligo plate respirometer (Supplementary
650 Information 1.3.4). Embryo were dissected from mothers and transferred to wells of a 24-well
651 plate, where their oxygen consumption was measured over 60 minutes. The measurement was
652 then repeated in media dosed with 5 μM rotenone to test sensitivity to Complex I inhibition, after
653 which the embryos were video recorded and photographed for morphometrics in ImageJ. We

654 used linear models to test the effect of *ndufs5* genotype, *ndufa13* genotype, and individual
655 standard length on a number of variables, controlling for batch effects (Supplementary
656 Information 1.3.4–1.3.5).
657
658 **Mitochondrial respirometry**
659 To further evaluate mitochondrial function in individuals heterozygous for the
660 mitonuclear incompatibility (Supplementary Information 1.3.6–1.3.7), we conducted
661 respirometry assays on *X. birchmanni*, *X. malinche*, and hybrid individuals that had the *X.*
662 *malinche* mitochondria and were heterozygous for the nuclear components of the hybrid
663 incompatibility (N=7 of each genotype). Mitochondria were isolated from whole liver tissue and
664 mitochondrial respiration was quantified using the Oroboros O2K respirometry system (Fig.
665 S30)[72]. A step-by-step description of this protocol and methods used to calculate respiratory flux
666 control factors is outlined in Supplementary Information 1.3.8. We complemented the results of
667 these respirometry experiments with measures of mitochondrial membrane potential using a flow
668 cytometry-based approach (Supplementary Information 1.3.9).
669
670 **Parallel reaction monitoring proteomics**
671 For Parallel Reaction Monitoring (PRM) with mass spectrometry, we used a similar
672 approach to that used for respirometry to isolate whole mitochondria from five F_1 hybrids (which
673 harbored *X. malinche* mitochondria). This approach is described in detail in Supplementary
674 Information 1.4.1. Briefly, we designed heavy-labeled peptides to distinguish between the *X.*
675 *birchmanni* and *X. malinche* copies of NDUFS5 and NDUFA13, facilitating quantification of the
676 peptides of interest in the mitochondrial proteome (Supplementary Information 1.4.2).

677 Mitochondrial isolates were prepared for mass spectrometry and combined with heavy-labeled
678 peptides in known quantities (see Supplementary Information 1.4.3), then submitted to Orbitrap
679 mass spectrometry with separation with UPLC and parallel reaction monitoring (PRM) for ion
680 selection. The protocol for mass spectrometry and PRM is described in detail in Supplementary
681 Information 1.4.4.

682 To analyze the results, the focal peptide's spectral peak were identified based on the peak
683 of the heavy labeled spike-in peptide. We focused analysis on the NDUFS5 peptide
684 WLL[L/P]QSGEQPYK since other endogenous peptides were below the expected sensitivity
685 limits of our PRM protocol (Supplementary Information 1.4.5). We normalized the intensity of
686 the NDUFS5 peptide based on the known spike-in quantity, and quantified the proportion of
687 NDUFS5 in each F_1 individual derived from *X. malinche* versus *X. birchmanni* (Supplementary
688 Information 1.4.5). We tested whether these ratios significantly deviated from the 50-50
689 expectation for F_1 hybrids using a two-sided one-sample *t*-test.

690

691 **Complex I protein modeling**

692 Mapping results allowed us to identify *ndufs5* and *ndufa13* as *X. birchmanni* genes that
693 interact negatively with *X. malinche* mitochondrial genes. We used a protein-modeling based
694 approach with RaptorX (http://raptorx.uchicago.edu) to identify the mitochondrial genes most
695 likely to interact with *ndufs5* and *ndufa13* (see Supplementary Information 1.4.6). Using the
696 mouse Cryo-EM structure (PDB ID 6G2J) of Complex I, we identified proteins in contact with
697 *ndufs5* and *ndufa13*, which included several mitochondrial (*nd2, nd3, nd4l, nd6*) and nuclear
698 (*ndufa1*, *ndufa8*, *ndufb5*, *ndufc2*) genes. We then used RaptorX to predict structures for both the

699 *X. birchmanni* and *X. malinche* versions of the proteins. In addition, we evaluated the robustness
700 of these predictions to choice of Cryo-EM template; see Supplementary Information 1.4.6.
701
702 **Analysis of evolutionary rates**
703 Comparison of predicted protein sequences from *ndufs5, ndufa13*, and mitochondrial
704 genes of interest (*nd2* and *nd6*) revealed a large number of substitutions between *X. birchmanni*
705 and *X. malinche*. We calculated d_N/d_S between *X. birchmanni* and *X. malinche* for all annotated
706 protein coding genes throughout the genome and found that both *ndufs5* and *ndufa13* have rapid
707 protein evolution (Fig. 4D; Supplementary Information 1.5.1). Examining these mutations in a
708 phylogenetic context revealed that many substitutions in *ndufs5*, *nudfa13*, and *nd6* were derived
709 in *X. birchmanni*. We tested for significant differences in evolutionary rates on the *X. birchmanni*
710 lineage and for predicted functional impacts of these substitutions; these analyses are described
711 in Supplementary Information 1.5.1.
712
713 **Tests for ancient introgression**
714 Previous work had indicated that the mitochondrial phylogeny in *Xiphophorus* is
715 discordant with the whole-genome species tree[37]. Specifically, although *X. birchmanni* and *X.*
716 *malinche* are sister species based on the nuclear genome, *X. malinche* and *X. cortezi* are sister
717 species based on the mitochondrial genome. We used a combination of PacBio amplicon
718 sequencing of 10 individuals (2 or more per species, Supplementary Information 1.5.3) and
719 newly available whole-genome resequencing data to confirm this result and polarize the direction
720 of the discordance by constructing maximum likelihood mitochondrial phylogenies with the
721 program RAxML[74]. We performed similar phylogenetic analyses of the nuclear genes that

722 interact with the *X. malinche* mitochondria (*ndufs5* and *ndufa13*; Supplementary Information
723 1.5.3). Combined with phylogenetic results, simulation results suggest that gene flow from *X.*
724 *malinche* into *X. cortezi* is the most likely cause of the discordance we observe between the
725 mitochondrial and nuclear phylogenies (Supplementary Information 1.5.3–1.5.4). Since *X.*
726 *malinche* and *X. cortezi* are not currently sympatric, this suggests ancient gene flow between
727 them (Supplementary Information 1.5.5).
728
729 **Contemporary hybridization between *X. birchmanni* and *X. cortezi***
730 To investigate the possibility that hybrids between *X. birchmanni* and *X. cortezi* share the
731 same mitonuclear incompatibility as observed in hybrids between *X. birchmanni* and *X. malinche*
732 (Supplementary Information 1.5.6), we took advantage of genomic data from recently discovered
733 hybrid populations between *X. birchmanni* and *X. cortezi*[75]. Using data from three different *X.*
734 *birchmanni* × *X. cortezi* populations and a permutation-based approach, we asked whether
735 ancestry at *ndufs5* and *ndufa13* showed lower mismatch with mitochondrial ancestry than
736 expected given the genome-wide ancestry distribution. This analysis is described in detail in
737 Supplementary Information 1.5.6.
738
739 **Animal Care and Use**
740 All methods were performed in compliance with Stanford Administrative Panel on Laboratory
741 Animal Care protocol #33071.
742
743
744

745 **Data Availability**

746 Raw sequencing reads used in this project are available under NCBI SRA Bioprojects
747 PRJNA744894, PRJNA746324, PRJNA610049, and PRJNA745218. Mass spectrometry data are
748 available on PRIDE (accession pending), and all other datasets necessary to recreate the results
749 of the publication are available on Dryad (accessions pending).

750

751 **Code Availability**

752 All new customs scripts used to generate results will be made available on Github at
753 https://github.com/Schumerlab/mitonuc_DMI and
754 https://github.com/Schumerlab/Lab_shared_scripts.

755 **References**

756 1. Dagilis, A. J., Kirkpatrick, M. & Bolnick, D. I. The evolution of hybrid fitness during
757 speciation. *PLOS Genetics* **15**, e1008125 (2019).
758 2. Dobzhansky, T. Genetic Nature of Species Differences. *Am Nat* **71**, 404–420 (1937).
759 3. Muller, H. Isolating mechanisms, evolution, and temperature. *Biological Symposium* **6**, 71–
760 125 (1942).
761 4. Maheshwari, S. & Barbash, D. A. The Genetics of Hybrid Incompatibilities. *Annu Rev Genet*
762 **45**, 331–355 (2011).
763 5. Presgraves, D. C. The molecular evolutionary basis of species formation. *Nat Rev Genet* **11**,
764 175–180 (2010).
765 6. Swamy, K. B. S., Schuyler, S. C. & Leu, J.-Y. Protein Complexes Form a Basis for Complex
766 Hybrid Incompatibility. *Front Genet* **12**, (2021).
767 7. Orr, H. A. The population genetics of speciation: the evolution of hybrid incompatibilities.
768 *Genetics* **139**, 1805–1813 (1995).
769 8. Boocock, J., Sadhu, M. J., Durvasula, A., Bloom, J. S. & Kruglyak, L. Ancient balancing
770 selection maintains incompatible versions of the galactose pathway in yeast. *Science* **371**,
771 415–419 (2021).
772 9. Wei, W.-H., Hemani, G. & Haley, C. S. Detecting epistasis in human complex traits. *Nat Rev*
773 *Genet* **15**, 722–733 (2014).
774 10. Gauderman, W. J. Sample size requirements for association studies of gene-gene interaction.
775 *Am J Epidemiol* **155**, 478–484 (2002).
776 11. Phadnis, N. *et al.* An essential cell cycle regulation gene causes hybrid inviability in
777 Drosophila. *Science* **350**, 1552–1555 (2015).

778 12. Tang, S. & Presgraves, D. C. Evolution of the Drosophila Nuclear Pore Complex Results in
779 Multiple Hybrid Incompatibilities. *Science* **323**, 779–782 (2009).
780 13. Cooper, J. C., Guo, P., Bladen, J. & Phadnis, N. A triple-hybrid cross reveals a new hybrid
781 incompatibility locus between D. melanogaster and D. sechellia. *bioRxiv* 590588 (2019)
782 doi:10.1101/590588.
783 14. Kuzmin, E. *et al.* Systematic analysis of complex genetic interactions. *Science* **360**, (2018).
784 15. Johnson, N. A. Hybrid incompatibility genes: remnants of a genomic battlefield? *Trends*
785 *Genet* **26**, 317–325 (2010).
786 16. Burton, R. S. & Barreto, F. S. A disproportionate role for mtDNA in Dobzhansky–Muller
787 incompatibilities? *Mol Ecol* **21**, 4942–4957 (2012).
788 17. Hill, G. E. Mitonuclear coevolution as the genesis of speciation and the mitochondrial DNA
789 barcode gap. *Ecol Evol* **6**, 5831–5842 (2016).
790 18. Ballard, J. W. O. & Whitlock, M. C. The incomplete natural history of mitochondria. *Mol*
791 *Ecol* **13**, 729–744 (2004).
792 19. Haag-Liautard, C. *et al.* Direct Estimation of the Mitochondrial DNA Mutation Rate in
793 Drosophila melanogaster. *PLOS Biol* **6**, e204 (2008).
794 20. Allio, R., Donega, S., Galtier, N. & Nabholz, B. Large Variation in the Ratio of
795 Mitochondrial to Nuclear Mutation Rate across Animals: Implications for Genetic Diversity
796 and the Use of Mitochondrial DNA as a Molecular Marker. *Mol Biol Evol* **34**, 2762–2772
797 (2017).
798 21. Barr, C. M., Neiman, M. & Taylor, D. R. Inheritance and recombination of mitochondrial
799 genomes in plants, fungi and animals. *New Phytol* **168**, 39–50 (2005).

800 22. Chase, C. D. Cytoplasmic male sterility: a window to the world of plant mitochondrial–
801 nuclear interactions. *Trends Genet* **23**, 81–90 (2007).
802 23. Case, A. L., Finseth, F. R., Barr, C. M. & Fishman, L. Selfish evolution of cytonuclear
803 hybrid incompatibility in Mimulus. *Proc R Soc Lond B* **283**, 20161493 (2016).
804 24. Lane, N. & Martin, W. The energetics of genome complexity. *Nature* **467**, 929–934 (2010).
805 25. Osada, N. & Akashi, H. Mitochondrial–Nuclear Interactions and Accelerated Compensatory
806 Evolution: Evidence from the Primate Cytochrome c Oxidase Complex. *Mol Biol Evol* **29**,
807 337–346 (2012).
808 26. Barreto, F. S. & Burton, R. S. Evidence for Compensatory Evolution of Ribosomal Proteins
809 in Response to Rapid Divergence of Mitochondrial rRNA. *Mol Biol Evol* **30**, 310–314
810 (2013).
811 27. Bolnick, D. I., Turelli, M., López-Fernández, H., Wainwright, P. C. & Near, T. J.
812 Accelerated Mitochondrial Evolution and "Darwin's Corollary": Asymmetric Viability of
813 Reciprocal F1 Hybrids in Centrarchid Fishes. *Genetics* **178**, 1037–1048 (2008).
814 28. Turelli, M. & Moyle, L. C. Asymmetric Postmating Isolation: Darwin's Corollary to
815 Haldane's Rule. *Genetics* **176**, 1059–1088 (2007).
816 29. Brandvain, Y., Pauly, G. B., May, M. R. & Turelli, M. Explaining Darwin's Corollary to
817 Haldane's Rule: The Role of Mitonuclear Interactions in Asymmetric Postzygotic Isolation
818 Among Toads. *Genetics* **197**, 743–747 (2014).
819 30. Tiffin, P., Olson, S. & Moyle, L. C. Asymmetrical crossing barriers in angiosperms. *Proc R*
820 *Soc Lond B* **268**, 861–867 (2001).

821 31. Meiklejohn, C. D. *et al.* An Incompatibility between a Mitochondrial tRNA and Its Nuclear-
822 Encoded tRNA Synthetase Compromises Development and Fitness in Drosophila. *PLOS*
823 *Genetics* **9**, e1003238 (2013).
824 32. Luo, D. *et al.* A detrimental mitochondrial-nuclear interaction causes cytoplasmic male
825 sterility in rice. *Nat Genet* **45**, 573–577 (2013).
826 33. Lee, H.-Y. *et al.* Incompatibility of Nuclear and Mitochondrial Genomes Causes Hybrid
827 Sterility between Two Yeast Species. *Cell* **135**, 1065–1073 (2008).
828 34. Hanson, M. R. & Bentolila, S. Interactions of Mitochondrial and Nuclear Genes That Affect
829 Male Gametophyte Development. *The Plant Cell* **16**, S154–S169 (2004).
830 35. Taylor, S. A. & Larson, E. L. Insights from genomes into the evolutionary importance and
831 prevalence of hybridization in nature. *Nat Ecol Evol* **3**, 170–177 (2019).
832 36. Edelman, N. B. & Mallet, J. Prevalence and Adaptive Impact of Introgression. *Annu Rev*
833 *Genet* **55**, 265–283 (2021).
834 37. Cui, R. *et al.* Phylogenomics reveals extensive reticulate evolution in *Xiphophorus* fishes.
835 *Evolution* **67**, 2166–2179 (2013).
836 38. Nelson, T. C. *et al.* Ancient and recent introgression shape the evolutionary history of
837 pollinator adaptation and speciation in a model monkeyflower radiation (Mimulus section
838 Erythranthe). *PLoS Genet* **17**, e1009095 (2021).
839 39. Buck, R. & Flores-Rentería, L. The Syngameon Enigma. *Plants* **11**, 895 (2022).
840 40. Schumer, M., Cui, R., Rosenthal, G. G. & Andolfatto, P. Reproductive Isolation of Hybrid
841 Populations Driven by Genetic Incompatibilities. *PLoS Genet* **11**, e1005041 (2015).
842 41. Culumber, Z. W. *et al.* Replicated hybrid zones of *Xiphophorus* swordtails along an
843 elevational gradient. *Mol Ecol* **20**, 342–356 (2011).

844 42. Fisher, H. S., Wong, B. B. M. & Rosenthal, G. G. Alteration of the chemical environment
845 disrupts communication in a freshwater fish. *Proc R Soc B* **273**, 1187–1193 (2006).
846 43. Schumer, M. *et al.* Natural selection interacts with recombination to shape the evolution of
847 hybrid genomes. *Science* **360**, 656–660 (2018).
848 44. Schumer, M. & Brandvain, Y. Determining epistatic selection in admixed populations. *Mol*
849 *Ecol* **25**, 2577–2591 (2016).
850 45. Schumer, M. *et al.* High-resolution mapping reveals hundreds of genetic incompatibilities in
851 hybridizing fish species. *eLife* **3**, e02535 (2014).
852 46. Powell, D. L. *et al.* Natural hybridization reveals incompatible alleles that cause melanoma
853 in swordtail fish. *Science* **368**, 731–736 (2020).
854 47. Powell, D. L. *et al.* The Genetic Architecture of Variation in the Sexually Selected Sword
855 Ornament and Its Evolution in Hybrid Populations. *Curr Biol* **31**, 923-935.e11 (2021).
856 48. Langdon, Q. K. *et al.* Predictability and parallelism in the contemporary evolution of hybrid
857 genomes. *PLoS Genet* **18**, e1009914 (2022).
858 49. Schartl, M. *et al.* The genome of the platyfish, Xiphophorus maculatus, provides insights into
859 evolutionary adaptation and several complex traits. *Nat Genet* **45**, 567–572 (2013).
860 50. Schumer, M., Powell, D. L. & Corbett-Detig, R. Versatile simulations of admixture and
861 accurate local ancestry inference with mixnmatch and ancestryinfer. *Mol Ecol Resour* **20**,
862 1141–1151 (2020).
863 51. Sharma, L. K., Lu, J. & Bai, Y. Mitochondrial Respiratory Complex I: Structure, Function
864 and Implication in Human Diseases. *Curr Med Chem* **16**, 1266–1277 (2009).
865 52. Haynes, J. L. Standardized Classification of Poeciliid Development for Life-History Studies.
866 *Copeia* **1995**, 147 (1995).

867 53. Tavolga, W. N. Embryonic development of the platyfish (Platypoecilus), the swordtail
868 (Xiphophorus), and their hybrids. Bulletin of the AMNH ; v. 94, article 4. *Embryonic*
869 *development in fish* (1949).
870 54. Byrnes, J. *et al.* Pharmacologic modeling of primary mitochondrial respiratory chain
871 dysfunction in zebrafish. *Neurochem Int* **117**, 23–34 (2018).
872 55. Pinho, B. R. *et al.* How mitochondrial dysfunction affects zebrafish development and
873 cardiovascular function: an in vivo model for testing mitochondria-targeted drugs. *Br J*
874 *Pharmacol* **169**, 1072–1090 (2013).
875 56. González-Quintana, A. *et al.* Novel NDUFA13 Mutations Associated with OXPHOS
876 Deficiency and Leigh Syndrome: A Second Family Report. *Genes (Basel)* **11**, 855 (2020).
877 57. McElroy, G. S. *et al.* NAD+ Regeneration Rescues Lifespan, but Not Ataxia, in a Mouse
878 Model of Brain Mitochondrial Complex I Dysfunction. *Cell Metab* **32**, 301-308.e6 (2020).
879 58. McElroy, G. S. *et al.* Reduced expression of mitochondrial complex I subunit Ndufs2 does
880 not impact healthspan in mice. *Sci Rep* **12**, 5196 (2022).
881 59. Agip, A.-N. A. *et al.* Cryo-EM structures of complex I from mouse heart mitochondria in
882 two biochemically defined states. *Nat Struct Mol Biol* **25**, 548–556 (2018).
883 60. Kampjut, D. & Sazanov, L. A. The coupling mechanism of mammalian respiratory complex
884 I. *Science* **370**, (2020).
885 61. Fiedorczuk, K. *et al.* Atomic structure of the entire mammalian mitochondrial complex I.
886 *Nature* **538**, 406–410 (2016).
887 62. Mack, K. L. & Nachman, M. W. Gene Regulation and Speciation. *Trends Genet* **33**, 68–80
888 (2017).

889 63. Källberg, M. *et al.* Template-based protein structure modeling using the RaptorX web server.
890 *Nature Protocols* **7**, 1511–1522 (2012).
891 64. Formosa, L. E., Dibley, M. G., Stroud, D. A. & Ryan, M. T. Building a complex complex:
892 Assembly of mitochondrial respiratory chain complex I. *Semin Cell Dev Biol* **76**, 154–162
893 (2018).
894 65. Hill, G. E. Mitonuclear Compensatory Coevolution. *Trends Genet* **36**, 403–414 (2020).
895 66. Sloan, D. B., Havird, J. C. & Sharbrough, J. The on-again, off-again relationship between
896 mitochondrial genomes and species boundaries. *Mol Ecol* **26**, 2212–2236 (2017).
897 67. Ellison, C. K. & Burton, R. S. Disruption of Mitochondrial Function in Interpopulation
898 Hybrids of Tigriopus Californicus. *Evolution* **60**, 1382–1391 (2006).
899 68. Ellison, C. K., Niehuis, O. & Gadau, J. Hybrid breakdown and mitochondrial dysfunction in
900 hybrids of Nasonia parasitoid wasps. *J Evol Biol* **21**, 1844–1851 (2008).
901 69. Olson, J. R., Cooper, S. J., Swanson, D. L., Braun, M. J. & Williams, J. B. The Relationship
902 of Metabolic Performance and Distribution in Black-Capped and Carolina Chickadees.
903 *Physiol Biochem Zool* **83**, 263–275 (2010).
904 70. Lu, Y. *et al.* Oncogenic allelic interaction in Xiphophorus highlights hybrid incompatibility.
905 *PNAS* **117**, 29786–29794 (2020).
906 71. Corbett-Detig, R. & Nielsen, R. A Hidden Markov Model Approach for Simultaneously
907 Estimating Local Ancestry and Admixture Time Using Next Generation Sequence Data in
908 Samples of Arbitrary Ploidy. *PLOS Genetics* **13**, e1006529 (2017).
909 72. Chung, D. J., Bryant, H. J. & Schulte, P. M. Thermal acclimation and subspecies-specific
910 effects on heart and brain mitochondrial performance in a eurythermal teleost (Fundulus
911 heteroclitus). *J Exp Biol* **220**, 1459–1471 (2017).

912 73. Ng, P. C. & Henikoff, S. SIFT: predicting amino acid changes that affect protein function.
913 *Nucleic Acids Res* **31**, 3812–3814 (2003).
914 74. Stamatakis, A. RAxML-VI-HPC: Maximum likelihood-based phylogenetic analyses with
915 thousands of taxa and mixed models. *Bioinformatics* **22**, 2688–2690 (2006).
916 75. Powell, D. L. *et al.* Two new hybrid populations expand the swordtail hybridization model
917 system. *Evolution* **75**, 2524–2539 (2021).
918

Acknowledgements

We thank Peter Andolfatto, Stepfanie Aguillon, Yaniv Brandvain, Jenn Coughlan, Hunter Fraser, Yuki Haba, Nitin Phadnis, Molly Przeworski, Ken Thompson and members of the Schumer lab for helpful discussion and/or feedback on earlier versions of this manuscript. We thank Alexa Pollock for help performing rotenone trials. We thank the Federal Government of Mexico for permission to collect fish. Stanford University and the Stanford Research Computing Center provided computational support for this project. We thank the Vincent Coates Foundation Mass Spectrometry Laboratory, Stanford University Mass Spectrometry (RRID:SCR_017801) for technical and experimental support. **Funding:** This work was supported by a Knight-Hennessy Scholars fellowship and NSF GRFP 2019273798 to B. Moran, a CEHG fellowship and NSF PRFB (2010950) to Q. Langdon, NIH P30 CA124435 in utilizing the Stanford Cancer Institute Proteomics/Mass Spectrometry Shared Resource, NIH grant 1R35GM142836 to J. Havird, and a Hanna H. Gray fellowship, Sloan Fellowship, and NIH grant 1R35GM133774 to M. Schumer.

Author Contributions: B.M.M., D.L.P, and M. Schu, designed the project; B.M.M., C.Y.P., E.N.K.I., S.M.B, A.E.D, A.M, J.J.B, K.K., F.L., R.M., K.S., O.H.-P., J.C.H., A. M. and M. Schu. collected data; B.M.M., C.Y.P., Q.L.K., F.L., J.C.H., A.M., and M. Schu. performed analyses; D.L.P., T.R.G., R.D.L., C.G., R.C.-D., J.F. and M. Scha. provided expertise and technical support.

Competing Interests: the authors declare no competing interests.

Materials & Correspondence: correspondence and requests for materials should be directed to B.M.M. (benmoran@stanford.edu) or M. Schu (schumer@stanford.edu).